ACSNANO

www.acsnano.org

ARTICLE

Nonlinear Tunable Vibrational Response in Hexagonal Boron Nitride

Fadil Iyikanat, Andrea Konečná, and F. Javier García de Abajo*

Cite This: *ACS Nano* 2021, 15, 13415−13426

Read Online

ACCESS | Metrics & More | Article Recommendations

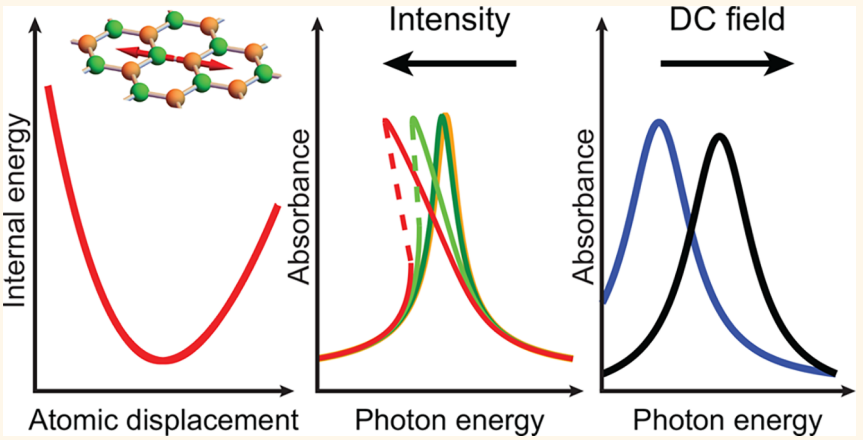

ABSTRACT: **Nonlinear light−matter interactions in structured materials are the source of exciting properties and enable vanguard applications in photonics. However, the magnitude of nonlinear effects is generally small, thus requiring high optical intensities for their manifestation at the nanoscale. Here, we reveal a large nonlinear response of monolayer hexagonal boron nitride (hBN) in the mid-infrared phonon−polariton region, triggered by the strongly anharmonic potential associated with atomic vibrations in this material. We present robust first-principles theory predicting a threshold light field ∼24 MV/m to produce order-unity effects in Kerr nonlinearities and harmonic generation, which are made possible by a combination of the long lifetimes exhibited by optical phonons and the strongly asymmetric landscape of the configuration energy in hBN. We further foresee polariton blockade at the few-quanta level in nanometer-sized structures. In addition, by mixing static and optical fields, the strong nonlinear response of monolayer hBN gives rise to substantial frequency shifts of optical phonon modes, exceeding their spectral width for in-plane DC fields that are attainable using lateral gating technology. We therefore predict a practical scheme for electrical tunability of the vibrational modes with potential interest in mid-infrared optoelectronics. The strong nonlinear response, low damping, and robustness of hBN polaritons set the stage for the development of applications in light modulation, sensing, and metrology, while triggering the search for an intense vibrational nonlinear response in other ionic materials.**

KEYWORDS: *nonlinear response, phonon polaritons, quantum optics, hexagonal boron nitride, mid-infrared spectroscopy*

Major improvements in nanofabrication[1−3] and colloid and surface chemistry[4,5] over the past two decades have enabled an extraordinary degree of control over the electromagnetic field associated with light at nanometer scales, well below the free-space light wavelength. These advances have facilitated the development of applications in fields such as optoelectronics,[6] optical sensing,[7−9] photochemistry,[10] and light harvesting[11] by exploiting the linear optical response of the involved materials. In addition, nonlinear effects offer a wealth of possibilities in quantum optics,[12] harmonic generation,[13] all-optical light modulation and switching,[14,15] and nonlinear microscopy[16−20] and

Received: May 4, 2021
Accepted: July 15, 2021
Published: July 26, 2021

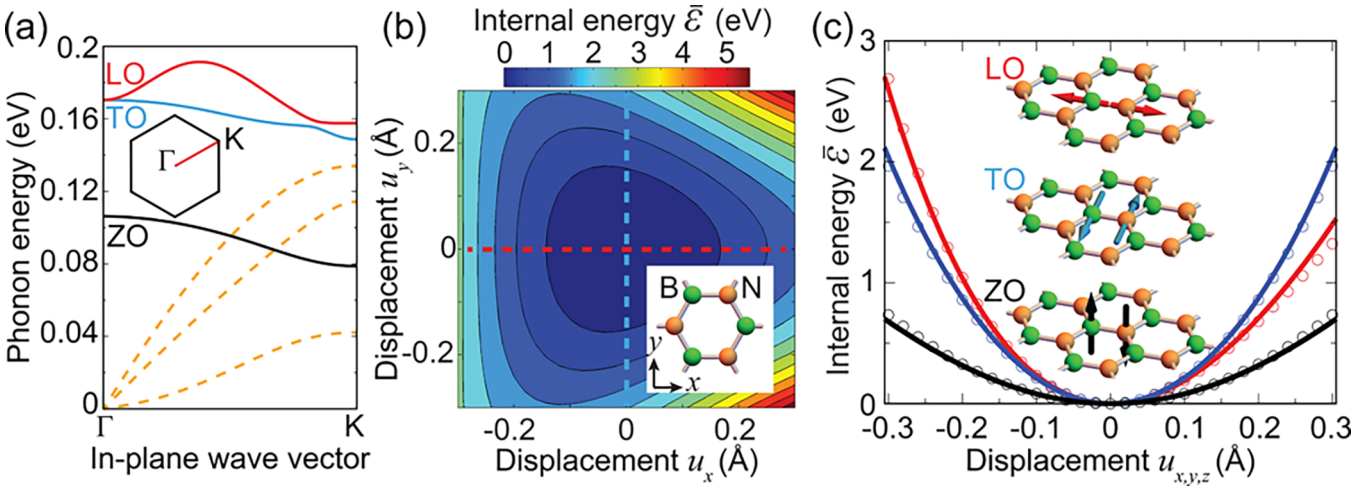

Figure 1. Anharmonicity in the atomic vibrations of monolayer hBN. (a) Linear dispersion relations of the three acoustic (dashed curves) and three optical (ZO, TO, and LO solid curves) phonon modes along the Γ−K direction (see first Brillouin zone in the inset) calculated from DFT (see the Methods section). (b) Total internal energy per unit cell as a function of in-plane relative B−N atomic displacement u at the Γ point. We set the energy origin at the equilibrium configuration u = 0. (c) Color-coded cuts along the dashed lines in part b. For comparison, we also show the energy variation associated with out-of-plane motion (ZO mode, black curve and lowest inset). We plot DFT results (symbols) and polynomial fits (curves, see the main text). The plot reveals strong nonparabolicity for motion along *x* (LO mode).

sensing.[8,21−24] Unfortunately, the nonlinear response of available materials is rather weak, so the manifestation of nonlinear phenomena generally demands their accumulation as light propagates across large structures (*i.e.*, extending over many optical wavelengths[14,15]) or, alternatively, the use of intense optical fields. However, the light intensity that can be tolerated by nanostructures is limited due to heating damage, which can be effectively prevented by reducing the irradiation time, so understandably, progress in nonlinear optics has largely relied on the availability of ultrafast laser pulses with fluences $\lesssim$10 J/m^2. Two-level atoms constitute the paramount example of a nonlinear system[14] in which resonant photon absorption is prevented after it is formerly excited by a previous photon. However, individual atoms possess small transition strengths, as quantified by the f-sum rule,[25] because roughly only one electron is effectively involved in the excitation, thus resulting in poor coupling to light and, consequently, also a weak nonlinear response. Insulators and semiconductor materials can exhibit a larger transition strength associated with a higher density of available valence electrons, and actually, there are notable examples among them offering a relatively large nonlinear response combined with low optical absorption that enable applications such as optical parameter oscillators for frequency conversion.[14] The high density of conduction electrons in metals also translates into a larger transition strength, which, although accompanied by substantial optical absorption, still gives rise to relatively strong nonlinearities, particularly in noble metal nanostructures.[26−30]

Localized optical resonances can produce amplification of the externally applied light intensity to enhance nonlinear effects.[31] In particular, metal plasmons provide the means to amplify the near field intensity by several orders of magnitude, thus strongly increasing the nonlinear response.[29,32−39] Unfortunately, metals suffer from large optical losses[40] that limit their lifetimes, so alternative less lossy materials have been explored, such as graphene, which can sustain electrically tunable[41,42] and long-lived[43] plasmons, while simultaneously featuring a strong nonlinear response because of the conic, anharmonic nature of its electronic band structure.[44,45] More precisely, graphene exhibits a large third-order susceptibility that manifests in relatively strong four-wave mixing,[46−48] third-harmonic generation (THG),[49−52] and the optical Kerr effect.[53,54] Although graphene plasmons have been only observed at low frequencies in the terahertz and mid-infrared domains, they can enhance the intrinsically large nonlinear response of their host material,[52,55] with potential applications in quantum optics[12] and high-harmonic generation.[56]

The two-dimensionality of graphene is advantageous for nanophotonic devices because it facilitates exposure to the external optical field. Likewise, the vast family of two-dimensional (2D) transition metal dichalcogenides (TMDs) also hosts interesting nonlinear properties, as revealed by the observation of strong second-harmonic generation (SHG) in odd-layer films of MoS_2,[57,58] $MoSe_2$,[59] WS_2,[60] and WSe_2,[61] as well as THG in MoS_2[62,63] and spiral WS_2.[64]

For sufficiently strong external fields, atomic vibrations in solids and molecules can be pushed beyond the harmonic regime, thus exhibiting a nonlinear behavior. Surprisingly, harmonic generation associated with atomic vibrations has only been poorly explored, with just a few works focusing on this phenomenon at terahertz frequencies,[65−68] as well as a parallel effort on parametric amplification of optical phonons in SiC.[69] The strength of vibrational nonlinear effects is a key question that determines the range of applications, but this line of research is still open, in search of robust materials with an intense response. Mid-infrared nanophotonic devices would benefit from such strong nonlinearity, in particular in 2D platforms that enable easy access to the external field. In this context, hexagonal boron nitride (hBN) emerges as an appealing candidate that exhibits long-lived optical phonon polaritons, although their associated nonlinear response has not yet been assessed.

Here, we find that atomic vibrations in polar crystals can produce strong optical nonlinearities in the mid-infrared spectral region, on par with their electronic counterparts in strongly nonlinear media. We concentrate on monolayer hBN as a material of current interest due to its ability to host long-lived phonon polaritons at spectral bands emerging at around

https://doi.org/10.1021/acsnano.1c03775
ACS Nano 2021, 15, 13415−13426

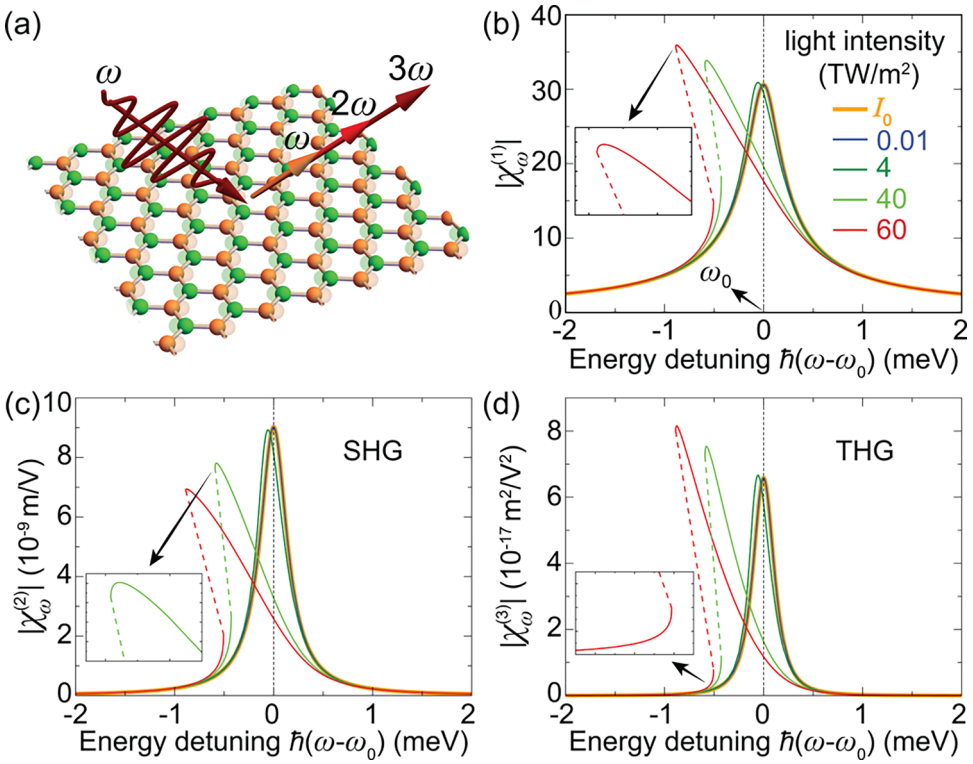

Figure 2. Nonlinear optical response of monolayer hBN in the upper optical-phonon region. (a) We consider normally impinging light with linear polarization along one of the B−N bond directions *x*. Spectral dependence of the susceptibilities $\chi_\omega^{(s)}$ associated with the fundamental (b), SHG (c), and THG (d) frequencies (s = 1−3, respectively) for a series of increasing incident light intensities (see legend in part b). We show the low-intensity perturbative limit χ_ω^{ss} for comparison (thick orange curves). The photon energy $\hbar\omega$ refers to the linear mode resonance ($\hbar\omega_0 \approx 170$ meV). We assume a phonon lifetime given by $\tau = 2$ ps (*i.e.*, $\hbar\tau^{-1} \approx 0.33$ meV).

∼100 and ∼170 meV, as demonstrated in recent studies of thin layers.[70−73] Through first-principles simulations, we find that the higher-energy band exhibits a substantial degree of asymmetry for atomic vibrations involving stretching of the B−N bond, giving rise to a strongly anharmonic behavior that translates into relatively intense harmonic generation as well as sizable Kerr nonlinearity. Phonon polaritons such as those in hBN therefore emerge as a promising platform for mid-infrared nonlinear optics, with applications that include harmonic generation, optical modulation, and quantum blockade at the few-quantum level in nanometer-sized structures as well as active electrical modulation by applying DC lateral fields.

RESULTS AND DISCUSSION

The dispersion diagram of monolayer hBN phonons contains three relatively high-energy optical-phonon bands, one starting at ∼106 meV (ZO) and the other two above ∼170 meV (TO and LO), associated with atomic vibrations primarily involving motion perpendicular and parallel to the hexagonal atomic lattice plane, respectively. In this paper, we study vibrations at the Γ point, where the two upper bands are degenerate (Figure 1a). Our treatment is exact when dealing with normally impinging light, but we argue that it also provides a good approximation to model strongly confined phonon−polaritons with in-plane wavelengths down to $\lambda_p \sim 10$ nm, whose associated wave vectors $2\pi/\lambda_p \sim 0.06$ Å^{-1} are small compared with the wave vector at the K point $4\pi/3\sqrt{3}\,a \approx 1.7$ Å^{-1}, where $a = 1.446$ Å is the B−N bond distance. We thus expect that the linear and nonlinear response functions derived from the present Γ-point analysis embody an accurate description of the optical properties of mid-infrared phonon−polaritons in monolayer hBN.

At the Γ point, atoms in each crystal unit cell follow the same vibration pattern, which can be described in terms of the B−N relative displacement vector $\mathbf{u}$ according to the equation of motion (see the Methods section)

$$M[\ddot{\mathbf{u}}(t) + \tau^{-1}\dot{\mathbf{u}}(t)] = -\nabla_{\mathbf{u}}[\bar{\mathcal{E}}(\mathbf{u}) - \bar{\mathbf{p}}(\mathbf{u})\cdot\mathbf{E}^{\text{ext}}(t)] \quad (1)$$

where $M = M_B M_N/(M_B + M_N)$ is the reduced mass, $\bar{\mathcal{E}}(\mathbf{u})$ and $\bar{\mathbf{p}}(\mathbf{u})$ are the displacement-dependent configuration energy and dipole per unit cell, respectively, $\mathbf{E}^{\text{ext}}(t)$ is the electric field of the external light, and we introduce a phenomenological lifetime τ. For concreteness, we take the B−N bond vector along x with the B and N unit-cell atoms placed at $a\hat{\mathbf{x}}$ and $2a\hat{\mathbf{x}}$, respectively. For a given $\mathbf{u}$, the displacements of the two unit cell atoms are $\mathbf{u}_B = -(M/M_B)\mathbf{u}$ and $\mathbf{u}_N = (M/M_N)\mathbf{u}$ (*i.e.*, positive u_x corresponds to stretching), where $M_B = 10.811$ Da and $M_N = 14.007$ Da are the average masses corresponding to the natural isotopic abundances of these two elements. In what follows, we set $\tau = 2$ ps, which is consistent with the lifetimes observed in optical measurements.[74] In addition, we calculate $\bar{\mathcal{E}}(\mathbf{u})$ and $\bar{\mathbf{p}}(\mathbf{u})$ using density-functional theory (DFT), as explained in the Methods section. Because we focus on the Γ point, atomic displacements preserve translational crystal symmetry, so DFT methods for infinite crystals can be straightforwardly applied. We concentrate on the upper optical phonon branches, associated with in-plane atomic motion (*i.e.*, $u_z = 0$). Retaining only up to quartic terms in $\bar{\mathcal{E}}$ and cubic terms in $\bar{\mathbf{p}}$ compatible with mirror symmetry relative to the

https://doi.org/10.1021/acsnano.1c03775
ACS Nano 2021, 15, 13415−13426

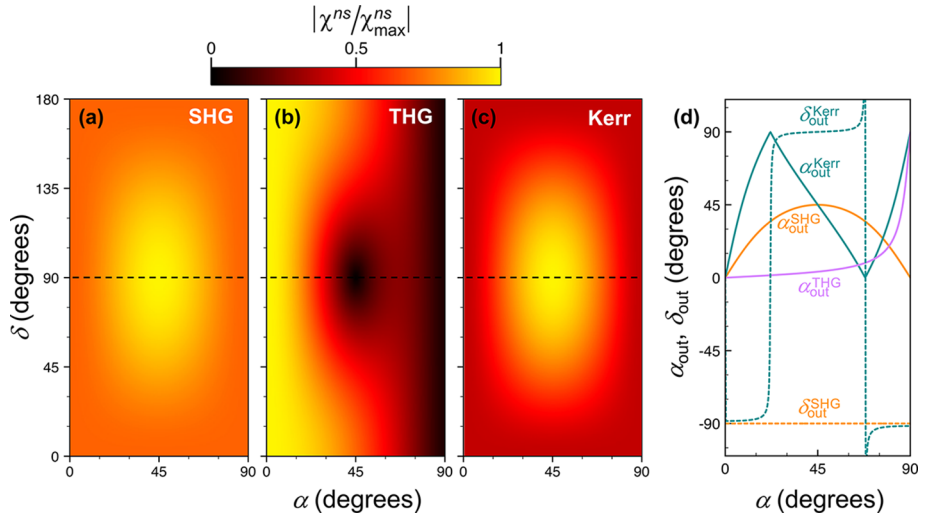

Figure 3. Polarization dependence of the nonlinear response. (a–c) Perturbative results for the dependence of the nonlinear susceptibility associated with SHG, THG, and the Kerr effect on the polarization of the external light under normal incidence on monolayer hBN. The polarization angles define the field amplitude as $\cos(\alpha)\hat{\mathbf{x}} + \sin(\alpha)e^{i\delta}\hat{\mathbf{y}}$. Maxima in the color scale correspond to $\chi^{22}_{max} = 1.3 \times 10^{-8}$ m/V, $\chi^{33}_{max} = 6.6 \times 10^{-17}$ m²/V², and $\chi^{31}_{max} = 3.6 \times 10^{-14}$ m²/V² for the SHG (a), THG (b), and Kerr (c) susceptibilities, assuming a polariton lifetime $\tau = 2$ ps. (d) Polarization angles of the output nonlinear components as a function of α for $\delta = 90°$ (*i.e.*, along the dashed lines in parts a–c).

$u_y = 0$ line and 3-fold crystal symmetry around $\hat{z}$, our DFT calculations for $u \leq 0.03$ Å lead to the fitted expressions

$$\bar{\mathcal{E}}(\mathbf{u}) \approx e_0(u_x^2 + u_y^2) + e_1 u_x(u_x^2 - 3u_y^2) + e_2 u^4 \tag{2a}$$

$$\bar{\mathbf{p}}(\mathbf{u}) \approx \bar{p}_0\hat{\mathbf{x}} + Q_0\mathbf{u} + Q_1[(u_x^2 - u_y^2)\hat{\mathbf{x}} - 2u_x u_y\hat{\mathbf{y}}] + Q_2 u^2\mathbf{u} \tag{2b}$$

with coefficients $e_0 = 0.2175$, $e_1 = -0.1126$, $e_2 = 0.0488$, $\bar{p}_0 = -1.1001$, $Q_0 = -0.4981$, $Q_1 = -0.0014$, and $Q_2 = -0.7552$ expressed in atomic units. We note that $\mathbf{p}(\mathbf{u})$ is accompanied by the external field in eq 1, so both of the expansions in eqs 2a and 2b account for corrections up to the third order in the external field. As a result of the crystal symmetries noted above, the energy landscape (Figure 1b) exhibits a more anharmonic profile for motion along x, as clearly observed when comparing cuts across $u_x = 0$ and $u_y = 0$ (Figure 1c). For completeness, we calculate (with coefficients in atomic units) $\bar{\mathcal{E}} \approx 0.0839u_z^2 - 0.0167u_z^4$ and $\bar{p}_z \approx -0.304u_z + 0.194u_z^3$ for out-of-plane motion at $u_x = u_y = 0$; these expressions reveal a more harmonic potential (*i.e.*, smaller nonlinear effects) and a light-coupling dipole of similar strength in the ZO mode.

Equations 2 encapsulate all the information that is needed to study the vibrational dynamics driven by external illumination in the spectral region near the upper optical modes at the Γ point according to eq 1. In particular, the corresponding unperturbed in-plane mode energy $\hbar\omega_0 = \hbar\sqrt{2e_0/M} \approx 170$ meV is in excellent agreement with previous theoretical[75] and experimental[76,77] results. Incidentally, the permanent dipole $\bar{p}_0$ does not affect optical phonons at the Γ point, although it contributes to the dynamics of acoustic modes.

In what follows, we study the response to a monochromatic external field $\mathbf{E}^{ext}(t) = 2\mathbf{E}_0\cos(\omega t)$ of frequency ω by solving eq 1 either perturbatively or numerically in the time domain, thus yielding the time-dependent displacement vector $\mathbf{u}(t)$ and from here the unit-cell induced dipole $\bar{\mathbf{p}}(\mathbf{u}) - \bar{\mathbf{p}}(0)$, from which we extract the nonlinear response functions of monolayer hBN.

Nonperturbative Nonlinear Response in Monolayer hBN. Based on the energy landscapes shown in Figure 1b,c, we expect a strong nonlinear response associated with atomic vibrations for in-plane displacement vectors oriented along x (the unit-cell B–N bond direction). Because this is a symmetry axis, such vibrations are rigorously constrained to $u_y = u_z = 0$ if the external field is also oriented along x, so inserting eqs 2a and 2b into eq 1 and plugging external monochromatic light of frequency ω, the equation of motion reduces to

$$\ddot{u}_x + \tau^{-1}\dot{u}_x + \omega_0^2 u_x + (3e_1/M)u_x^2 + (4e_2/M)u_x^3 = (2/M)(Q_0 + 2Q_1 u_x + 3Q_2 u_x^2)E_0\cos(\omega t) \tag{3}$$

which is a generalization of the Duffing equation.[78] In Figure 2, we present results obtained by numerically integrating this equation as a function of ω for different levels of light intensity $I_0 = 2E_0^2/Z_0$, where $Z_0 = \sqrt{\mu_0/\epsilon_0} \approx 376.73\ \Omega$ is the vacuum impedance. From the solution for the time-dependent displacement $u_x(t)$, we express the induced dipole (eq 2b) as $p_x(t) = Q_0 u_x(t) + Q_1 u_x^2(t) + Q_2 u_x^3(t)$. In practice, we solve the above differential equation starting from some initial boundary conditions (see below) and integrating up to a large time $t = N\tau_\omega \gg \tau$ (expressed as a multiple of the optical period $\tau_\omega = 2\pi/\omega$), so that the transient response produced after plugging the external light is attenuated to a negligible level. We then compute the susceptibility associated with a harmonic s as

$$\chi_\omega^{(s)} = \frac{1}{\epsilon_0(E_0)^s\mathcal{V}\tau_\omega}\int_{N\tau_\omega}^{(N+1)\tau_\omega} dt\ p_x(t)e^{is\omega t} \tag{4}$$

where ϵ_0 is the vacuum permittivity, and we divide by a volume $\mathcal{V} = \mathcal{A}h$ given by the product of the unit cell area $\mathcal{A} = (3\sqrt{3}/2)a^2 = 5.43$ Å² and the layer thickness $h = 3.3$

https://doi.org/10.1021/acsnano.1c03775
ACS Nano 2021, 15, 13415–13426

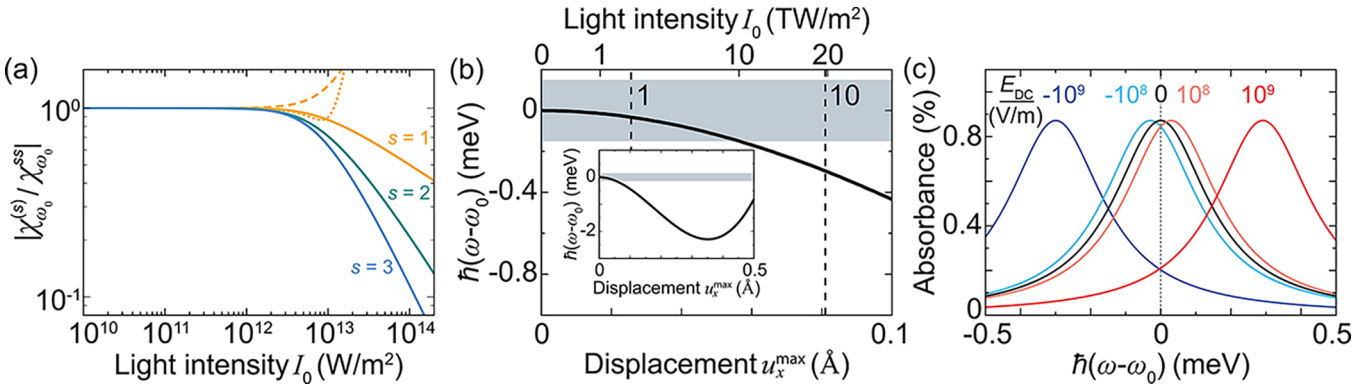

Figure 4. Nonlinear saturation of the optical response. (a) On-resonance susceptibilities $\chi^{(s)}_{\omega_0}$ associated with the fundamental (s = 1), SHG (s = 2), and THG (s = 3) response as a function light intensity I_0 under the conditions of Figure 2, normalized to the low-I_0 limit $\chi^{ss}_{\omega_0}$. Analytical perturbative results are shown as broken curves, including the contribution of $\chi^{31}_{\omega_0}$ (dashed curve) and $\chi^{51}_{\omega_0}$ (dotted curve). (b) Amplitude dependence of the in-plane vibration frequency for motion along x. The lower horizontal axis corresponds to the maximum displacement, while the upper axis indicates the light intensity needed to reach it according to Figure 2b. The two dashed vertical lines indicate the $\sqrt{2}$ times the rms displacement in a ~1 nm² island (18 unit cells) for a phonon population of 1 and 10 phonons, as indicated by labels. The shaded region indicates an fwhm corresponding to a lifetime τ = 2 ps. (c) Spectral change in the linear absorbance spectrum of monolayer hBN produced by a uniform in-plane DC field along x for different values of the field amplitudes.

Å, with the latter approximated to the interatomic plane distance in bulk hBN.

At low intensities, the susceptibilities exhibit a Lorentzian profile of decreasing width as the harmonic order s increases. Our numerical results converge well to the perturbative analytical limit (see the Methods section) for $I_0 \to 0$ (thick orange curves in Figure 2b–d). When the intensity increases, the spectral peak is redshifted, and eventually, we reach a region of bistability. We explore this behavior by using the converged solution for each ω as the initial condition to calculate the response for a slightly different ω; this leads to two branches, corresponding to increasing or decreasing frequency paths starting from −2 or 2 meV detuning, respectively. Such behavior is observed for all harmonics investigated in Figure 2. In the bistability region, a third unstable branch exists,[14] which we illustrate by dashed lines, introduced here as a guide to the eye. Nonperturbative effects are perceptible for light intensities $I_0 \gtrsim 3$ TW/m² (*i.e.*, $E_0 \gtrsim 24$ MV/m).

Polarization Dependence. The in-plane anisotropy of hBN translates into a strong dependence of the nonlinear response on light polarization, which we analyze in Figure 3. Specifically, we represent the perturbative susceptibilities associated with SHG, THG, and the Kerr effect (see the Methods section) for normally impinging light of frequency $\omega = \omega_0$ tuned to the in-plane Γ phonon frequency as a function of polarization angles (α, δ), defined in such a way that the incident field amplitude vector is proportional to $\cos(\alpha)\hat{\mathbf{x}} + \sin(\alpha)e^{i\delta}\hat{\mathbf{y}}$. The second-harmonic response (Figure 3a) is independent of the direction of the field amplitude for linear polarization (δ = 0), while an absolute maximum is observed for circularly polarized light (CPL, α = 45°, δ = 90°) with a relative enhancement of 41%. Interestingly, the polarization of the SHG signal under CPL irradiation is reversed (output polarization angles α_{out} = 45°, δ_{out} = −90°; see Figure 3d). We find that THG (Figure 3b) reaches a maximum for polarization along x (δ = 0), where it is completely depleted for CPL, in agreement with the intuitive conclusions extracted from the anharmonicity observed in Figure 1c for oscillations parallel or perpendicular with respect to the B–N bond direction. We also analyze the third-order Kerr susceptibility (Figure 3c), which is maximal for CPL, in which case the polarization angles of the nonlinear Kerr response are the same as the incident ones (Figure 3d). Incidentally, right on resonance ($\omega = \omega_0$), we find that $\chi^{31}_{\omega_0}$ is 90° out of phase relative to both $\chi^{11}_{\omega_0}$ and $\chi^{51}_{\omega_0}$ (see the Methods section), so the relative correction to the polarization intensity coming from the Kerr effect scales with the incident intensity as I_0^2, with contributions at that order arising from both $\mathrm{Re}\{\chi^{11*}_{\omega_0}\chi^{51}_{\omega_0}\}$ (*i.e.*, through mixing with the linear amplitude) and $|\chi^{31}_{\omega_0}|^2$. This translates into a dependence of $|\chi^{(1)}|^2$ on I_0 as shown in Figure 4a (see also the discussion in the Methods section), where the lowest-order correction (dashed curve for s = 1, obtained by including $\chi^{31}_{\omega_0}$) leads to the wrong sign in the variation of the first-harmonic intensity, whereas the addition of χ^{51} (dotted curve) produces an initial depletion, in agreement with the nonperturbative result (solid curve), although this approximation eventually breaks down for a larger incident intensity.

Saturation and Quantum Blockade. The onset of saturation at ~3 TW/m² is illustrated in Figure 4a, where we plot the susceptibilities associated with polarization emerging at the fundamental, SHG, and THG frequencies for on-resonance illumination at $\omega = \omega_0$. Saturation occurs faster as the harmonic order increases because this involves higher powers of the fundamental field amplitude. From a physical viewpoint, this plot essentially describes the combination of anharmonic oscillations and the effective coupling strength to external light. We find the first of these factors to be of interest *per se* because it affects the departure from harmonic behavior at the few-quanta level. In fact, this is the basis for the quantum blockade phenomenon, which we mentioned above for two-level systems: for a sufficiently anharmonic response, the energy of a two-quanta state differs from twice the energy of one quantum. Quantum blockade has been observed in cavity quantum electrodynamics experiments, whereby a two-level atom is coupled to an optical cavity,[79] so that the system

https://doi.org/10.1021/acsnano.1c03775
ACS Nano 2021, 15, 13415–13426

inherits a strong anharmonicity from the former, as well as a large coupling to light from the latter. Incidentally, this type of effect has also been theoretically studied with graphene–plasmon cavities,[80] a configuration in which Rabi vacuum splitting can be discernible,[81] with a view to realizing quantum-optics devices in a solid-state environment by benefiting from the strong nonlinearity of this material. However, the fabrication of few-nanometer-sized graphene structures capable of sustaining high-quality plasmons remains an experimental challenge.

Atomic vibrations in monolayer hBN provide an excellent alternative to realize quantum blockade in compact structures, such as hBN nanoislands achievable through chemical[82,83] and physical methods,[84] which can profit from the structural stability of this material, as well as from the long lifetime and optical strength of its phonon polaritons. We explore this possibility by estimating the oscillation frequency associated with a given maximum displacement (Figure 4b) (see the Methods section). Larger oscillation amplitudes initially lead to frequency redshifts as a result of the reduction in the interatomic potential relative to a perfect parabola, quantified through the $e_1 < 0$ term in eq 2a. We also indicate in this figure an estimate for the root-mean-square (rms) amplitude associated with the in-plane optical phonon mode in a ∼1 nm^2 hBN island (18 unit cells) for an occupation of either 1 or 10 phonons (see the Methods section; the rms amplitude is proportional to $\sqrt{n/A}$, where n is the phonon occupation number, and A is the area of the island). Incidentally, we multiply the rms displacement by $\sqrt{2}$ to compare with the maximum displacement used in the horizontal axis of Figure 4b. The latter produces a frequency shift that exceeds the fwhm of the resonance assuming a lifetime $\tau = 2$ ps, therefore indicating the onset of quantum blockade.

Electrical Tunability. A lateral DC field acting on the hBN monolayer along x produces a change in the B–N bond distance to minimize energy. We argue that the strength of the in-plane DC field that can be applied through lateral gating can reach ∼10^9 V/m, as shown in experiments,[85] which is 1 order of magnitude larger than the maximum optical field considered in Figure 2. Still, a resonant optical field of amplitude $2E_0\cos(\omega_0 t)$ induces a maximum atomic displacement $\approx(2Q_0\tau/M\omega_0)E_0$ assisted by the amplifying mechanism of spring motion, while the displacement due to a DC field of the same magnitude is a factor of $\omega_0\tau \sim 500$ smaller. Nevertheless, we show next that the effect is strong enough to shift the phonon resonance by more than its spectral width, therefore enabling a practical route toward electrical light modulation that could find applications in optoelectronics. We start our analysis from eq 3 by substituting the applied field by $E_{DC} + 2E_0\cos(\omega_0 t)$. The DC component E_{DC} can be readily absorbed in a new set of parameters ω_0, e_1, Q_0, and Q_1, from which only the variation of ω_0 produces a sizable effect. Obviously, no constant force term can remain in eq 3, a condition from which we find an equilibrium displacement $u_x^0 \approx Q_0 E_{DC}/M\omega_0^2$. Because of the lack of parabolicity of the confining potential (see Figure 2c), we expect a shift in the resonance frequency of in-plane phonons at the Γ point; after some algebra, we find $\Delta\omega_0 \approx (3Q_0 e_1/M\omega_0^2 - 2Q_1)E_{DC}/M\omega_0$, which is linear in the DC field and reaches ∼0.26 meV for $E_{DC} \sim 10^9$ V/m. We also find that E_{DC}^2 corrections amount to less than 1%, whereas the linear and nonlinear optical responses of the material just experience a rigid frequency shift by $\Delta\omega_0$, with their magnitudes remaining nearly unaffected. This is illustrated by examining the absorbance of monolayer hBN ($\approx(4\pi\epsilon_0 h\omega/c)\mathrm{Im}\{\chi_\omega^{(1)}\}$), which reveals a peak shift by nearly twice the spectral width when the DC field is varied in the $\pm 10^9$ V/m range (Figure 4c). Therefore, we anticipate that lateral gating can be used as an efficient mechanism for light modulation in the mid-infrared regime using hBN vibrational modes.

CONCLUSIONS

In conclusion, we reveal monolayer hBN as an excellent nonlinear material at frequencies determined by its optical phonons. We base our results on first-principles predictive theory for the potential energy surface and induced dipole density in the material as a function of atomic positions. The optical response associated with atomic vibrations in monolayer hBN contains a substantial anharmonic component that gives rise to relatively intense second- and third-harmonic generation, as well as Kerr nonlinearity, as we show in comparison to existing experimental results for other 2D materials (Figure 5). We stress the fact that, in contrast to the nonlinear response arising from the electronic degrees of freedom, atomic vibrations offer a more robust platform with a lower level of optical losses. In particular, hBN can be compared with graphene, which operates in the same spectral range but suffers from intrinsic losses that limit the external light intensities that can be applied without producing material damage. Atomic vibrations in hBN are indeed immune to strong optical absorption, such as that taking place in metallic systems, which leads to an elevation of the electronic temperature and an associated change in the optical response (*i.e.*, an incoherent form of nonlinearity) that can mask and reduce the strength of coherent effects. Although graphene shows a larger nonlinear response associated with electronic degrees of freedom (Figure 5), we find hBN to be second best, and we argue that the vibrational origin of its optical response should permit elevating the applied light intensity without substantially increasing optical losses. It is also interesting to

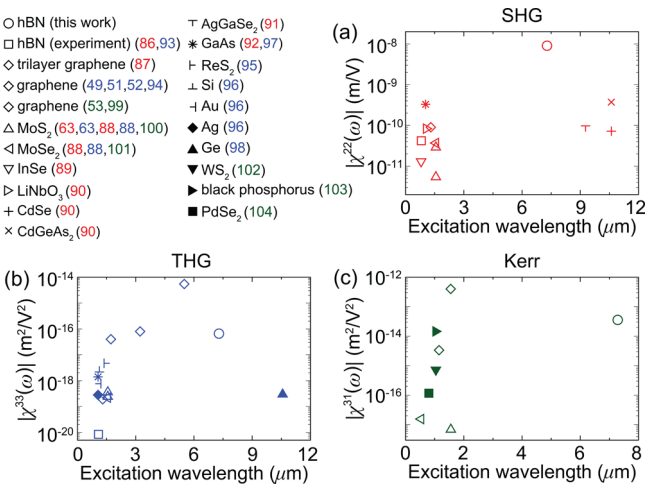

Figure 5. The nonlinear optical response of hBN in context. We compare the SHG, THG, and Kerr effect susceptibilities measured in different materials[49,51−53,63,86−104] (see color- and symbol-matching reference numbers in the legends) with our calculations for monolayer hBN at the in-plane Γ phonon frequency.

https://doi.org/10.1021/acsnano.1c03775
ACS Nano 2021, 15, 13415−13426

examine the ratio of nonlinear-to-linear susceptibilities (*e.g.*, $\mathcal{R} = |\chi^{31}/\chi^{11}|$), which reduces to

$$\mathcal{R}_{\mathrm{hBN}} = (6Q_0^2\tau^3/M^3\omega_0^3)|5e_1^2/M\omega_0^2 - 2e_2|$$

in monolayer hBN under resonant conditions (see eqs 7 in the Methods section) and $\mathcal{R}_{\mathrm{graphene}} = (3/8)(ev_F/E_F\omega_0)^2$ in doped graphene.[105] For an attainable Fermi energy E_F = 0.5 eV, a photon energy $\hbar\omega_0$ = 170 meV, and an hBN lifetime τ = 2 ps, we find $\mathcal{R}_{\mathrm{hBN}}/\mathcal{R}_{\mathrm{graphene}} \sim 20$, which reveals a substantially better performance of hBN. Incidentally, these ratios can be modified in both of these materials by the introduction of extrinsic resonating elements and also through intrinsic localized plasmon resonances in nanostructured graphene,[105] although edges in this material lead to additional losses that would compromise the overall nonlinear response. We have focused on vibrations around the in-plane optical mode frequency in hBN, but we anticipate that future studies will explore other materials, covering a wide range of mid-infrared frequencies, and possibly hosting strongly nonlinear vibrational resonances.

Edges in finite hBN islands and defects in actual samples can modify the phonon characteristics, for example, by producing localization at atomic scales,[106] which could affect the nonlinear response. Another interesting avenue consists in introducing strong in-plane DC fields to actively modify the nonlinear response, which we have predicted to enable phonon shifts exceeding their spectral width. In this respect, the insulator character of hBN should enable the presence of large lateral DC fields greatly exceeding those that are attainable through optical illumination. We have left aside thermal effects, which could also modify the nonlinear response, in particular in view of the fact that the in-plane mode population is ~1 at the melting temperature of hBN (>2900 K). The strong anharmonic response of hBN could be enhanced through resonant nanostructures,[31] a possibility that deserves further exploration to assess the prospects for mid-infrared nonlinear nanophotonics, which could benefit from the strong interest that this material is currently attracting in the scientific community.

The isotopic purity of the material influences the phonon lifetime τ (see Table 1 for the scaling with τ of the resonant susceptibility associated with different nonlinear processes) and thus requires further investigation in connection to nonlinear effects. In addition, we have made some emphasis on the separation between the intrinsic anharmonic motion (*i.e.*, the deviation in the potential energy surface from a parabolic profile) and the optical strength of the optical phonons (*i.e.*, the dipole moment associated with atomic displacements). While the overall nonlinear response is the combined result of both of these aspects, we argue that the former needs to be examined separately, as it controls the possibility of having quantum blockade, whereby subsequent excitation is prevented by the nonlinear effects produced in response to previous excitations. In monolayer hBN, we find that a nonlinear response at the few-quanta level is feasible by using structures of 1 nm lateral size, thus holding the potential for realizing quantum gates based on mid-infrared atomic vibrations in a robust solid-state material platform. In multilayer hBN crystals, the phonon frequency splits into more branches, whose nonlinear performance deserves further exploration, although we anticipate that only odd-layer samples should produce in-plane second-order nonlinearity; with monolayer stacks, lateral displacement and twisting could lead to interesting results also for even-order nonlinearities. We hope that the present study will stimulate the search for other vibrational materials in which the combination of long phonon lifetime, strong dipole moment, and large deviation from harmonic motion could give rise to a stronger nonlinear optical response in the mid-infrared.

Table 1. Peak Nonlinear Susceptibility in the Perturbative Regime[a]

ω_{in}	(n, s)	$s\omega_{\mathrm{in}}$	$\chi^{ns}_{\omega_{\mathrm{in}}}$	$\lvert\chi^{ns}_{\omega_{\mathrm{in}}}\rvert$ $(\mathrm{m}^{n-1}/\mathrm{V}^{n-1})$
ω_0	(1, 1)	ω_0	$\propto\tau$	30.6
ω_0	(2, 2)	$2\omega_0$	$\propto\tau^2$	9.03×10^{-9}
ω_0	(3, 3)	$3\omega_0$	$\propto\tau^3$	6.58×10^{-17}
ω_0	(3, 1)	ω_0	$\propto\tau^4$	1.39×10^{-14}
$\omega_0/2$	(2, 2)	ω_0	$\propto\tau$	9.46×10^{-11}
$\omega_0/2$	(3, 3)	$3\omega_0/2$	$\propto\tau$	3.48×10^{-22}
$\omega_0/3$	(3, 3)	ω_0	$\propto\tau$	1.25×10^{-21}

[a]We focus on polarization along the x direction (parallel to B−N bonds) and consider different incoming light frequencies ω_{in}, harmonics $s\omega_{\mathrm{in}}$, and perturbation orders n. The rightmost column shows the corresponding values of the susceptibilities in SI units for τ = 2 ps.

METHODS

Nonlinear Vibrational Optical Response. We examine the linear and nonlinear optical response associated with the atomic vibrations of monolayer hBN. The atomic scale under consideration is small compared with the light wavelength, so we work in the electrostatic limit and introduce the external light through an optical scalar potential $\phi^{\mathrm{ext}}(\mathbf{r}, t)$ acting on the B and N atoms (labeled by an index l), which oscillate around their equilibrium positions with time-dependent displacements $\mathbf{u}_l(t)$. For each configuration, defined by the set of the atomic displacements $\{\mathbf{u}\}$, we use DFT to calculate both the internal energy $\mathcal{E}(\{\mathbf{u}\})$ and the charge density distribution $\rho(\{\mathbf{u}\}, \mathbf{r})$ (see below). Adopting the Born−Oppenheimer approximation to separate electronic and vibrational motions, and describing the latter classically, we write the Lagrangian of the system as

$$\mathcal{L} = (1/2)\sum_l M_l|\dot{\mathbf{u}}_l(t)|^2 - \mathcal{E}(\{\mathbf{u}\}) - \int \mathrm{d}^3\mathbf{r}\,\rho(\{\mathbf{u}\}, \mathbf{r})\,\phi^{\mathrm{ext}}(\mathbf{r}, t)$$

where M_l denotes the mass of atom l, whereas the integral term stands for the potential energy due to the interaction with the external potential. From the Lagrange equation $\partial_t\nabla_{\dot{\mathbf{u}}_l}\mathcal{L} = \nabla_{\mathbf{u}_l}\mathcal{L}$, we find

$$M_l[\ddot{\mathbf{u}}_l(t) + \tau^{-1}\dot{\mathbf{u}}_l(t)] = -\nabla_{\mathbf{u}_l}\left[\mathcal{E}(\{\mathbf{u}\}) + \int \mathrm{d}^3\mathbf{r}\,\rho(\{\mathbf{u}\}, \mathbf{r})\,\phi^{\mathrm{ext}}(\mathbf{r}, t)\right] \quad (5)$$

where we have introduced a phenomenological lifetime τ (=2 ps in our calculations).

In the linear regime, we can approximate $\nabla_{\mathbf{u}_l}\mathcal{E}(\{\mathbf{u}\}) \approx \sum_{l'}\mathcal{D}_{ll'}\cdot\mathbf{u}_{l'}$ around the equilibrium configuration $\{\mathbf{u} = 0\}$, where $\mathcal{D}_{ll'}$ is the so-called dynamical matrix. The eigenvalues of this matrix define the phonon dispersion relations, as presented in Figure 1a for monolayer hBN based on our DFT calculations for $\mathcal{D}_{ll'}$ (see below).

The wave vectors associated with far-field light or even tip-based illumination ($\sim 1/R_{\mathrm{tip}} < 0.1$ nm^{-1} for a typical tip radius $R_{\mathrm{tip}} > 10$ nm) are at least 2 orders of magnitude smaller than the reciprocal lattice vectors ($\geq 4\pi/3a \approx 29$ nm^{-1}, where a = 1.446 Å is the B−N bond distance), so for applications in photonics, we are generally interested in atomic vibrations close to the Γ point (see Figure 1a). We thus study vibrations at this point as a good approximation to understand the nonlinear polaritonic dynamics in hBN. Under these conditions, the two atoms in each unit cell (B and N) move in the same way

https://doi.org/10.1021/acsnano.1c03775
ACS Nano 2021, 15, 13415−13426

across the crystal, and therefore, we only need to consider a central unit cell with the atom label l taking the values B or N. Clearly, the total potential (the quantity in square brackets in the right-hand side of eq 5) only depends on the relative coordinate $\mathbf{u} = \mathbf{u}_N - \mathbf{u}_B$, whereas the center of mass moves at constant velocity. We thus have $\mathbf{u}_B = -(M/M_B)\mathbf{u} \approx -0.564\mathbf{u}$ and $\mathbf{u}_N = (M/M_N)\mathbf{u} \approx 0.436\mathbf{u}$, where $M = M_B M_N/(M_B + M_N) \approx 6.102$ Da is the reduced mass (assuming naturally abundant isotope distributions), while the equation of motion becomes

$$M[\ddot{\mathbf{u}}(t) + \tau^{-1}\dot{\mathbf{u}}(t)] = -\nabla_{\mathbf{u}}\left[\bar{\mathcal{E}}(\mathbf{u}) + \int_{UC} d^3\mathbf{r}\, \rho(\mathbf{u}, \mathbf{r})\, \phi^{ext}(\mathbf{r}, t)\right] \tag{6}$$

Here, $\rho(\mathbf{u}, \mathbf{r})$ has the periodicity of the crystal, so the integral only extends over one unit cell (UC). Also, $\bar{\mathcal{E}}(\mathbf{u})$ is the internal energy per unit cell, which we obtain from DFT (see below). Finally, based on the smallness of the wave vectors accessed through external illumination, we can approximate $\phi^{ext}(\mathbf{r}, t) = -\mathbf{E}^{ext}(t)\cdot\mathbf{r}$ in terms of an external electric field $\mathbf{E}^{ext}(t)$, which allows us to rewrite eq 6 as in eq 1, where $\bar{\mathbf{p}}(\mathbf{u}) = \int_{UC} d^3\mathbf{r}\, \rho(\mathbf{u}, \mathbf{r})\, \mathbf{r}$ is the unit cell dipole. In this work, we simulate the nonlinear response of monolayer hBN in the in-plane phonon spectral region by solving eq 1 together with the DFT-based parametrization given in eqs 2a and 2b for $\bar{\mathcal{E}}(\mathbf{u})$ and $\bar{\mathbf{p}}(\mathbf{u})$.

DFT Calculations. We use the Vienna *ab initio* simulation package (VASP)[107−109] to carry out first-principles DFT calculations adopting the projector-augmented-wave (PAW) method[110] together with the generalized gradient approximation of Perdew−Burke−Ernzerhof (GGA-PBE) for the exchange-correlation functional.[111] A vacuum spacing of 10 Å between adjacent images is introduced to prevent artificial interactions. The plane-wave energy cutoff is set to 500 eV. We use the conjugate gradient method to optimize the structure with an energy convergence criterion of 10^{-8} eV between two ionic steps. A Γ-centered wave-vector sampling grid of size 18 × 18 × 1 is used for the structural relaxation. Atomic positions and lattice vectors are relaxed until the total force in the unit cell is reduced to a value below 10^{-7} eV/Å. The calculated B−N bond distance differs by just +0.3% from the measured value in bulk hBN. To obtain the charge density $\rho(\mathbf{u}, \mathbf{r})$, we calculate the electron densities corresponding to each atomic displacement using a sufficiently dense grid in the unit cell. The contribution from the nuclei and the K-shell electrons is incorporated by assimilating them to point charges ($3e$ for B and $5e$ for N), which add a term $\bar{\mathbf{p}}^{nucl}(\mathbf{u}) = 13ea\hat{\mathbf{x}} + eM(5/M_N - 3/M_B)\mathbf{u}$ to the unit cell dipole $\bar{\mathbf{p}}(\mathbf{u}) = \bar{\mathbf{p}}^{el}(\mathbf{u}) + \bar{\mathbf{p}}^{nucl}(\mathbf{u})$, where $\bar{\mathbf{p}}^{el}(\mathbf{u})$ originates in the 8 outer electrons per unit cell. The result from this analysis for in-plane atomic displacements is well described by the polynomial expressions in eqs 2a and 2b, which are compatible with the crystal symmetries of the hBN monolayer. The linear phonon frequencies and the dynamical matrix are calculated using the small displacement method.

Perturbation Limit. We find a perturbative solution to eq 1 by expanding the displacement vector as $\mathbf{u} = \sum_{ns}\mathbf{u}^{ns}e^{-is\omega t}$, where n is the scattering order, and s is the harmonic, subject to the condition $|s| \le n$. For a monochromatic field $\mathbf{E}^{ext}(t) = 2\mathbf{E}_0\cos(\omega t)$, this leads to the recurrence relation

$$\begin{aligned}
M[\omega_0^2 - s\omega(s\omega + i\tau^{-1})]u_i^{ns} &= -e_1\sum_{jk}\sum_{n's'} a_{ijk}u_j^{n's'}u_k^{n-n',s-s'} \\
&\quad - e_2\sum_{jkl}\sum_{n's'n''s''} b_{ijkl}u_j^{n's'}u_k^{n''s''}u_l^{n-n'-n'',s-s'-s''} \\
&\quad + Q_0\delta_{n,1}(\delta_{s,1}E_{0,i} + \delta_{s,-1}E_{0,i}^*) \\
&\quad + Q_1\sum_j c_{ijk}(u_j^{n-1,s-1}E_{0,k} + u_j^{n-1,s+1}E_{0,k}^*) \\
&\quad + Q_2\sum_{jkl}\sum_{n's'} d_{ijkl}u_j^{n's'}(u_k^{n-n'-1,s-s'-1}E_{0,l} + u_k^{n-n'-1,s-s'+1}E_{0,l}^*)
\end{aligned}$$

where $i, j, k, l \in \{x, y, z\}$ denote Cartesian components, and the only nonzero coefficients inside the sums (extracted from eqs 2a and 2b) are $a_{xxx} = -a_{yxy}/2 = -a_{xyy} = 3$, $b_{xxxx} = b_{xxyy} = b_{yyxx} = b_{yyyy} = 4$, $c_{xxx} = -c_{yyx} = -c_{xyy} = -c_{yxy} = 2$, $d_{xxxx} = d_{yyyy} = 3$, $d_{yxyx} = d_{xxyy} = 2$, and $d_{xyyx} = d_{yxxy} = 1$. Incidentally, this equation leads to the vanishing of u_i^{ns} if $n + s$ is odd. Through iterative solution, we obtain the displacement components u_i^{ns}, which upon insertion into eq 2b, also produce analytical expressions for the induced dipole. In particular, for incident polarization along x, the displacement vectors are found to be confined along x as well, and we obtain the perturbation series

$$\frac{p_x(t)}{\epsilon_0\mathcal{V}} = \sum_s \chi_\omega^{(s)}E_0^s e^{-is\omega t}$$

for the polarization density, where we define the field-dependent harmonic susceptibilities $\chi_\omega^{(s)} = \sum_n \chi_\omega^{ns}|E_0|^{n-s}$, which should coincide with eq 4. For incidence frequency near ω_0, the leading terms in the perturbation series are those involving the higher powers in the resonant factor $[\omega_0^2 - \omega(\omega + i\tau^{-1})]^{-1}$, namely

$$\chi_\omega^{11} \approx \frac{Q_0^2}{\epsilon_0\mathcal{V}M}\frac{1}{\omega_0^2 - \omega(\omega + i\tau^{-1})} \tag{7a}$$

$$\chi_\omega^{22} \approx \frac{Q_0^3}{\epsilon_0\mathcal{V}M^2}\left(\frac{e_1}{M\omega_0^2} + \frac{Q_1}{Q_0}\right)\frac{1}{[\omega_0^2 - \omega(\omega + i\tau^{-1})]^2} \tag{7b}$$

$$\chi_\omega^{33} \approx \frac{iQ_0^4}{4\epsilon_0\mathcal{V}M^4\omega_0^2}\left(2e_2 + \frac{8e_1Q_1}{Q_0} + \frac{3e_1^2}{M\omega_0^2} + \frac{4MQ_2\omega_0^2}{Q_0}\right)\frac{1}{[\omega_0^2 - \omega(\omega + i\tau^{-1})]^3} \tag{7c}$$

$$\chi_\omega^{31} \approx \frac{6Q_0^4}{\epsilon_0\mathcal{V}M^4}\left(\frac{5e_1^2}{M\omega_0^2} - 2e_2\right)\frac{1}{[\omega_0^2 - \omega(\omega + i\tau^{-1})]^2|\omega_0^2 - \omega(\omega + i\tau^{-1})|^2} \tag{7d}$$

These expressions are in excellent agreement with the numerical solution of the equation of motion (eq 1) for low field intensity (see Figure 2). Their scaling with the lifetime τ is summarized in Table 1, along with explicit values at $\omega = \omega_0$.

Incidentally, for the on-resonance Kerr effect, we have $\chi_{\omega_0}^{(1)} = \chi_{\omega_0}^{11} + \chi_{\omega_0}^{31}|E_0|^2 + \chi_{\omega_0}^{51}|E_0|^4 + \ldots$, contributed by odd-order susceptibilities

$$\begin{aligned}
\chi_{\omega_0}^{11} &= \frac{iQ_0^2\tau}{\epsilon_0\mathcal{V}M\omega_0} \\
\chi_{\omega_0}^{31} &= -\frac{6Q_0^4\tau^4}{\epsilon_0\mathcal{V}M^4\omega_0^4}(5e_1^2/M\omega_0^2 - 2e_2) \\
\chi_{\omega_0}^{51} &= -\frac{36iQ_0^6\tau^7}{\epsilon_0\mathcal{V}M^7\omega_0^7}(5e_1^2/M\omega_0^2 - 2e_2)^2
\end{aligned} \tag{8}$$

The $n = 3$ term is 90° out of phase with respect to $n = 1$, and thus, these two do not interfere in the resulting intensity $I^{(1)} \propto |\chi_{\omega_0}^{(1)}|^2$. Actually, for low E_0, the $n = 3$ contribution produces an increase in $I^{(1)}$, which is however compensated by the $n = 5$ term (see Figure 4a and the discussion in the main text). Nevertheless, for sufficiently off-resonance ω, the perturbative result embodied in eq 7d reproduces the decay of the curves in Figure 2b away from the resonance (not shown).

Phonon Quantization and Quantum Blockade. In the linear regime, the potential energy can be approximated by the quadratic expression $\mathcal{E}(\{\mathbf{u}\}) = (1/2)\sum_{ll'}\mathbf{u}_l\cdot\mathcal{D}_{ll'}\cdot\mathbf{u}_{l'}$, so in the absence of external illumination, the solution to the classical equation of motion (eq 5) admits an expansion $\mathbf{u}_l = M_l^{-1/2}\sum_n c_n\mathbf{e}_{nl}$ in terms of a

https://doi.org/10.1021/acsnano.1c03775
ACS Nano 2021, 15, 13415−13426

complete ($\sum_n \mathbf{e}_{nl} \otimes \mathbf{e}_{nl'} = \delta_{ll'}\mathcal{I}_3$) and orthonormal ($\sum_l \mathbf{e}_{nl}\cdot\mathbf{e}_{n'l} = \delta_{nn'}$) basis set of eigenvectors $\mathbf{e}_{nl}$ of the real, symmetric dynamical matrix (*i.e.*, $\sum_{l'} (M_l M_{l'})^{-1/2}\mathcal{D}_{ll'}\cdot\mathbf{e}_{nl'} = \omega_n^2\mathbf{e}_{nl}$, where ω_n are real oscillation eigenfrequencies). In a quantum description, we can write the Hamiltonian associated with atomic vibrations in general as $\hat{\mathcal{H}} = -\sum_l \hbar^2\nabla^2_{\mathbf{u}_l}/2M_l + \mathcal{E}(\{\mathbf{u}\}) = (1/2)\sum_n(-\hbar^2\partial^2_{c_n c_n} + \omega_n^2 c_n^2)$, where the rightmost expression, obtained by replacing the displacement vectors by the expansion coefficients $c_n = \sum_l \sqrt{M_l}\,\mathbf{e}_{nl}\cdot\mathbf{u}_l$, consists of a sum over quantum harmonic oscillators. Following a standard second quantization procedure, we interpret c_n and $-i\hbar\partial_{c_n}$ as displacement and momentum operators, respectively, from which we define phonon creation and annihilation operators $\hat{b}_n^\dagger$ and $\hat{b}_n$ through $c_n = \sqrt{\hbar/(2\omega_n)}\,(\hat{b}_n^\dagger + \hat{b}_n)$ and $-i\hbar\partial_{c_n} = i\sqrt{\hbar\omega_n/2}\,(\hat{b}_n^\dagger - \hat{b}_n)$, in terms of which the Hamiltonian reduces to $\hat{\mathcal{H}} = \hbar\sum_n \omega_n(\hat{b}_n^\dagger\hat{b}_n + 1/2)$. The rms displacement of atom l associated with the presence of one phonon in mode n is thus given by $\sqrt{\langle 0|\hat{b}_n|\mathbf{u}_l|^2\hat{b}_n^\dagger|0\rangle} = \sqrt{3\hbar/(2M_l\omega_n)}\,|\mathbf{e}_{nl}|$, where we have used the noted expansion of $\mathbf{u}_l$ in terms of eigenmodes and the expansion coefficients c_n in terms of ladder operators. For an hBN flake consisting of a finite number N of unit cells, approximating the eigenvectors to those of an infinite crystal, orthonormality implies $|\mathbf{e}_{nl}| \sim 1/\sqrt{N}$, and in particular, for oscillations at the Γ point, the rms displacement associated with one quantum reduces to $\sqrt{\langle u^2\rangle} \approx \sqrt{3\hbar/(2NM\omega_0)}$.

Oscillation Frequency beyond the Linear Regime. Focusing on atomic motion along x, we find the self-sustained oscillation frequency by multiplying eq 3 by the velocity $\dot{u}_x$, neglecting losses ($\tau^{-1} = 0$), and setting the external driving field to zero ($E_0 = 0$). As a function of the maximum displacement $u_x^{\max} > 0$ toward the positive x direction, where the potential is lower (see Figure 1a), direct integration then yields the oscillation period $T = 2\int_{u_x^{\min}}^{u_x^{\max}} du_x/\sqrt{f(u_x^{\max}) - f(u_x)}$, where $f(u_x) = \omega_0^2u_x^2 + (2e_1/M)u_x^3 + (2e_2/M)u_x^4$, and $u_x^{\min} < 0$ is the lower bound of the oscillation defined by $f(u_x^{\min}) = f(u_x^{\max})$. We find $u_x^{\min}$ from the analytical solution of the resulting polynomial of the fourth degree and then numerically integrate the above expression to obtain the oscillation frequency $\omega = 2\pi/T$, plotted in Figure 4b as a function of $u_x^{\max}$.

AUTHOR INFORMATION

Corresponding Author

F. Javier García de Abajo − *ICFO-Institut de Ciencies Fotoniques, The Barcelona Institute of Science and Technology, Castelldefels 08860 Barcelona, Spain; ICREA-Institució Catalana de Recerca i Estudis Avançats, 08010 Barcelona, Spain;* orcid.org/0000-0002-4970-4565; Email: javier.garciadeabajo@nanophotonics.es

Authors

Fadil Iyikanat − *ICFO-Institut de Ciencies Fotoniques, The Barcelona Institute of Science and Technology, Castelldefels 08860 Barcelona, Spain*

Andrea Konečná − *ICFO-Institut de Ciencies Fotoniques, The Barcelona Institute of Science and Technology, Castelldefels 08860 Barcelona, Spain;* orcid.org/0000-0002-7423-5481

Complete contact information is available at: https://pubs.acs.org/10.1021/acsnano.1c03775

Notes

The authors declare no competing financial interest.

ACKNOWLEDGMENTS

This work has been supported in part by the European Research Council (Advanced Grant 789104-eNANO), the Spanish MINECO (PID2020-112625GB-I00 and Severo Ochoa CEX2019-000910-S), the Catalan CERCA Program, and Fundaciós Cellex and Mir-Puig.

REFERENCES

(1) Nagpal, P.; Lindquist, N. C.; Oh, S.-H.; Norris, D. J. Ultrasmooth Patterned Metals for Plasmonics and Metamaterials. *Science* **2009**, *325*, 594−597.

(2) Duan, H.; Fernández-Domínguez, A. I.; Bosman, M.; Maier, S. A.; Yang, J. K. W. Nanoplasmonics: Classical down to the Nanometer Scale. *Nano Lett.* **2012**, *12*, 1683−1689.

(3) Davis, T. J.; Janoschka, D.; Dreher, P.; Frank, B.; Meyer zu Heringdorf, F.-J.; Giessen, H. Ultrafast Vector Imaging of Plasmonic Skyrmion Dynamics with Deep Subwavelength Resolution. *Science* **2020**, *368*, No. eaba6415.

(4) Burda, C.; Chen, X.; Narayanan, R.; El-Sayed, M. A. Chemistry and Properties of Nanocrystals of Different Shapes. *Chem. Rev.* **2005**, *105*, 1025−1102.

(5) Cai, J.; Ruffieux, P.; Jaafar, R.; Bieri, M.; Braun, T.; Blankenburg, S.; Muoth, M.; Seitsonen, A. P.; Saleh, M.; Feng, X.; Müllen, K.; Fasel, R. Atomically Precise Bottom-Up Fabrication of Graphene Nanoribbons. *Nature* **2010**, *466*, 470−473.

(6) Mak, K. F.; Shan, J. Photonics and Optoelectronics of 2D Semiconductor Transition Metal Dichalcogenides. *Nat. Photonics* **2016**, *10*, 216−226.

(7) Neumaier, P. F.-X.; Schmalz, K.; Borngräber, J.; Wylde, R.; Hübers, H.-W. Terahertz Gas-Phase Spectroscopy: Chemometrics for Security and Medical Applications. *Analyst* **2015**, *140*, 213−222.

(8) Di Fabrizio, E.; Schlücker, S.; Wenger, J.; Regmi, R.; Rigneault, H.; Calafiore, G.; West, M.; Cabrini, S.; Fleischer, M.; Van Hulst, N. F.; Garcia-Parajo, M. F.; Pucci, A.; Cojoc, D.; Hauser, C. A. E.; Ni, M. Roadmap on Biosensing and Photonics with Advanced Nano-Optical Methods. *J. Opt.* **2016**, *18*, 063003.

(9) Yang, X.; Sun, Z.; Low, T.; Hu, H.; Guo, X.; García de Abajo, F. J.; Avouris, P.; Dai, Q. Nanomaterial-Based Plasmon-Enhanced Infrared Spectroscopy. *Adv. Mater.* **2018**, *30*, 1704896.

(10) Clavero, C. Plasmon-Induced Hot-Electron Generation at Nanoparticle/Metal-Oxide Interfaces for Photovoltaic and Photocatalytic Devices. *Nat. Photonics* **2014**, *8*, 95−103.

(11) Atwater, H. A.; Polman, A. Plasmonics for Improved Photovoltaic Devices. *Nat. Mater.* **2010**, *9*, 205−213.

(12) Cox, J. D.; García de Abajo, F. J. Nonlinear Atom-Plasmon Interactions Enabled by Nanostructured Graphene. *Phys. Rev. Lett.* **2018**, *121*, 257403.

(13) Sivis, M.; Taucer, M.; Vampa, G.; Johnston, K.; Staudte, A.; Naumov, A. Y.; Villeneuve, D. M.; Ropers, C.; Corkum, P. B. Tailored Semiconductors for High-Harmonic Optoelectronics. *Science* **2017**, *357*, 303−306.

(14) Boyd, R. W. *Nonlinear Opt.*, 3rd ed.; Academic Press: Amsterdam, 2008.

(15) Garmire, E. Nonlinear Optics in Daily Life. *Opt. Express* **2013**, *21*, 30532−30544.

(16) Campagnola, P. J.; Loew, L. M. Second-Harmonic Imaging Microscopy for Visualizing Biomolecular Arrays in Cells, Tissues and Organisms. *Nat. Biotechnol.* **2003**, *21*, 1356−1360.

(17) Wang, Y.; Lin, C.-Y.; Nikolaenko, A.; Raghunathan, V.; Potma, E. O. Four-Wave Mixing Microscopy of Nanostructures. *Adv. Opt. Photonics* **2011**, *3*, 1−52.

(18) Dempsey, W. P.; Fraser, S. E.; Pantazis, P. SHG Nanoprobes: Advancing Harmonic Imaging in Biology. *BioEssays* **2012**, *34*, 351−360.

(19) Staedler, D.; Magouroux, T.; Hadji, R.; Joulaud, C.; Extermann, J.; Schwung, S.; Passemard, S.; Kasparian, C.; Clarke, G.; Gerrmann, M.; Dantec, R. L.; Mugnier, Y.; Rytz, D.; Ciepielewski, D.; Galez, C.; Gerber-Lemaire, S.; Juillerat-Jeanneret, L.; Bonacina, L.; Wolf, J.-P.

Harmonic Nanocrystals for Biolabeling: A Survey of Optical Properties and Biocompatibility. *ACS Nano* **2012**, *6*, 2542−2549.
(20) Huang, L.; Cheng, J.-X. Nonlinear Optical Microscopy of Single Nanostructures. *Annu. Rev. Mater. Res.* **2013**, *43*, 213−236.
(21) Neely, A.; Perry, C.; Varisli, B.; Singh, A. K.; Arbneshi, T.; Senapati, D.; Kalluri, J. R.; Ray, P. C. Ultrasensitive and Highly Selective Detection of Alzheimer's Disease Biomarker Using Two-Photon Rayleigh Scattering Properties of Gold Nanoparticle. *ACS Nano* **2009**, *3*, 2834−2840.
(22) Mesch, M.; Metzger, B.; Hentschel, M.; Giessen, H. Nonlinear Plasmonic Sensing. *Nano Lett.* **2016**, *16*, 3155−3159.
(23) Dhillon, S. S.; Vitiello, M. S.; Linfield, E. H.; Davies, A. G.; Hoffmann, M. C.; Booske, J.; Paoloni, C.; Gensch, M.; Weightman, P.; Williams, G. P.; Castro-Camus, E.; Cumming, D. R. S.; Simoens, F.; Escorcia-Carranza, I.; Grant, J.; Lucyszyn, S.; Kuwata-Gonokami, M.; Konishi, K.; Koch, M.; Schmuttenmaer, C. A.; et al. The 2017 Terahertz Science and Technology Roadmap. *J. Phys. D: Appl. Phys.* **2017**, *50*, 043001.
(24) Yu, R.; Cox, J. D.; García de Abajo, F. J. Nonlinear Plasmonic Sensing with Nanographene. *Phys. Rev. Lett.* **2016**, *117*, 123904.
(25) Pines, D.; Noziéres, P. *The Theory of Quantum Liquids*; W. A. Benjamin, Inc.: New York, 1966.
(26) Uchida, K.; Kaneko, S.; Omi, S.; Hata, C.; Tanji, H.; Asahara, Y.; Ikushima, A. J.; Tokizaki, T.; Nakamura, A. Optical Nonlinearities of a High Concentration of Small Metal Particles Dispersed in Glass: Copper and Silver Particles. *J. Opt. Soc. Am. B* **1994**, *11*, 1236−1243.
(27) Galletto, P.; Brevet, P. F.; Girault, H. H.; Antoine, R.; Broyer, M. Size Dependence of the Surface Plasmon Enhanced Second Harmonic Response of Gold Colloids: Towards a New Calibration Method. *Chem. Commun.* **1999**, 581−582.
(28) Russier-Antoine, I.; Benichou, E.; Bachelier, G.; Jonin, C.; Brevet, P. F. Multipolar Contributions of the Second Harmonic Generation from Silver and Gold Nanoparticles. *J. Phys. Chem. C* **2007**, *111*, 9044−9048.
(29) Liu, T.-M.; Tai, S.-P.; Yu, C.-H.; Wen, Y.-C.; Chu, S.-W.; Chen, L.-J.; Prasad, M. R.; Lin, K.-J.; Sun, C.-K. Measuring Plasmon-Resonance Enhanced Third-Harmonic $\chi^{(3)}$ of Ag Nanoparticles. *Appl. Phys. Lett.* **2006**, *89*, 043122.
(30) Singh, A. K.; Senapati, D.; Neely, A.; Kolawole, G.; Hawker, C.; Ray, P. C. Nonlinear Optical Properties of Triangular Silver Nanomaterials. *Chem. Phys. Lett.* **2009**, *481*, 94−98.
(31) Rodríguez Echarri, A.; Cox, J. D.; Yu, R.; García de Abajo, F. J. Enhancement of Nonlinear Optical Phenomena by Localized Resonances. *ACS Photonics* **2018**, *5*, 1521−1527.
(32) Lippitz, M.; van Dijk, M. A.; Orrit, M. Third-Harmonic Generation from Single Gold Nanoparticles. *Nano Lett.* **2005**, *5*, 799−802.
(33) Danckwerts, M.; Novotny, L. Optical Frequency Mixing at Coupled Gold Nanoparticles. *Phys. Rev. Lett.* **2007**, *98*, 026104.
(34) Schwartz, O.; Oron, D. Background-Free Third Harmonic Imaging of Gold Nanorods. *Nano Lett.* **2009**, *9*, 4093−4097.
(35) Butet, J.; Duboisset, J.; Bachelier, G.; Russier-Antoine, I.; Benichou, E.; Jonin, C.; Brevet, P.-F. Optical Second Harmonic Generation of Single Metallic Nanoparticles Embedded in a Homogeneous Medium. *Nano Lett.* **2010**, *10*, 1717−1721.
(36) Butet, J.; Bachelier, G.; Russier-Antoine, I.; Jonin, C.; Benichou, E.; Brevet, P.-F. Interference between Selected Dipoles and Octupoles in the Optical Second-Harmonic Generation from Spherical Gold Nanoparticles. *Phys. Rev. Lett.* **2010**, *105*, 077401.
(37) Stockman, M. I. Nanoplasmonics: Past, Present, and Glimpse into Future. *Opt. Express* **2011**, *19*, 22029−22106.
(38) Harutyunyan, H.; Volpe, G.; Quidant, R.; Novotny, L. Enhancing the Nonlinear Optical Response Using Multifrequency Gold-Nanowire Antennas. *Phys. Rev. Lett.* **2012**, *108*, 217403.
(39) Kauranen, M.; Zayats, A. V. Nonlinear Plasmonics. *Nat. Photonics* **2012**, *6*, 737−748.
(40) Khurgin, J. B. How to Deal with the Loss in Plasmonics and Metamaterials. *Nat. Nanotechnol.* **2015**, *10*, 2−6.
(41) Fei, Z.; Rodin, A. S.; Andreev, G. O.; Bao, W.; McLeod, A. S.; Wagner, M.; Zhang, L. M.; Zhao, Z.; Thiemens, M.; Dominguez, G.; Fogler, M. M.; Neto, A. H. C.; Lau, C. N.; Keilmann, F.; Basov, D. N. Gate-Tuning of Graphene Plasmons Revealed by Infrared Nano-Imaging. *Nature* **2012**, *487*, 82−85.
(42) Chen, J.; Badioli, M.; Alonso-González, P.; Thongrattanasiri, S.; Huth, F.; Osmond, J.; Spasenović, M.; Centeno, A.; Pesquera, A.; Godignon, P.; Zurutuza Elorza, A.; Camara, N.; García de Abajo, F. J.; Hillenbrand, R.; Koppens, F. H. L. Optical Nano-Imaging of Gate-Tunable Graphene Plasmons. *Nature* **2012**, *487*, 77−81.
(43) Ni, G. X.; McLeod, A. S.; Sun, Z.; Wang, L.; Xiong, L.; Post, K. W.; Sunku, S. S.; Jiang, B.-Y.; Hone, J.; Dean, C. R.; Fogler, M. M.; Basov, D. N. Fundamental Limits to Graphene Plasmonics. *Nature* **2018**, *557*, 530−533.
(44) Mikhailov, S. A. Non-Linear Electromagnetic Response of Graphene. *Europhys. Lett.* **2007**, *79*, 27002.
(45) Mikhailov, S. A.; Ziegler, K. Nonlinear Electromagnetic Response of Graphene: Frequency Multiplication and the Self-Consistent-Field Effects. *J. Phys.: Condens. Matter* **2008**, *20*, 384204.
(46) Hendry, E.; Hale, P. J.; Moger, J.; Savchenko, A. K.; Mikhailov, S. A. Coherent Non-Linear Optical Response of Graphene. *Phys. Rev. Lett.* **2010**, *105*, 097401.
(47) Gu, T.; Petrone, N.; McMillan, J. F.; van der Zande, A.; Yu, M.; Lo, G. Q.; Kwong, D. L.; Hone, J.; Wong, C. W. Regenerative Oscillation and Four-Wave Mixing in Graphene Optoelectronics. *Nat. Photonics* **2012**, *6*, 554−559.
(48) Constant, T. J.; Hornett, S. M.; Chang, D. E.; Hendry, E. All-Optical Generation of Surface Plasmons in Graphene. *Nat. Phys.* **2016**, *12*, 124−127.
(49) Kumar, N.; Kumar, J.; Gerstenkorn, C.; Wang, R.; Chiu, H.-Y.; Smirl, A. L.; Zhao, H. Third Harmonic Generation in Graphene and Few-Layer Graphite Films. *Phys. Rev. B: Condens. Matter Mater. Phys.* **2013**, *87*, No. 121406(R).
(50) Hong, S.-Y.; Dadap, J. I.; Petrone, N.; Yeh, P.-C.; Hone, J.; Osgood, R. M., Jr. Optical Third-Harmonic Generation in Graphene. *Phys. Rev. X* **2013**, *3*, 021014.
(51) Soavi, G.; Wang, G.; Rostami, H.; Purdie, D. G.; De Fazio, D.; Ma, T.; Luo, B.; Wang, J.; Ott, A. K.; Yoon, D.; Bourelle, S. A.; Muench, J. E.; Goykhman, I.; Dal Conte, S.; Celebrano, M.; Tomadin, A.; Polini, M.; Cerullo, G.; Ferrari, A. C. Broadband, Electrically Tunable Third-Harmonic Generation in Graphene. *Nat. Nanotechnol.* **2018**, *13*, 583−588.
(52) Calafell, I. A.; Rozema, L. A.; Iranzo, D. A.; Trenti, A.; Jenke, P. K.; Cox, J. D.; Kumar, A.; Bieliaiev, H.; Nanot, S.; Peng, C.; Efetov, D. K.; Kong, J.-Y.; Kong, J.; Englund, D. R.; García de Abajo, F. J.; Koppens, F. H. L.; Walther, P. Giant Enhancement of Third-Harmonic Generation in Graphene-Metal Heterostructures. *Nat. Nanotechnol.* **2021**, *16*, 318−324.
(53) Zhang, H.; Virally, S.; Bao, Q.; Ping, L. K.; Massar, S.; Godbout, N.; Kockaert, P. Z-Scan Measurement of the Nonlinear Refractive Index of Graphene. *Opt. Lett.* **2012**, *37*, 1856−1858.
(54) Dremetsika, E.; Dlubak, B.; Gorza, S.-P.; Ciret, C.; Martin, M.-B.; Hofmann, S.; Seneor, P.; Dolfi, D.; Massar, S.; Emplit, P.; Kockaert, P. Measuring the Nonlinear Refractive Index of Graphene Using the Optical Kerr Effect Method. *Opt. Lett.* **2016**, *41*, 3281−3284.
(55) Cox, J. D.; García de Abajo, F. J. Nonlinear Graphene Nanoplasmonics. *Acc. Chem. Res.* **2019**, *52*, 2536−2547.
(56) Cox, J. D.; Marini, A.; García de Abajo, F. J. Plasmon-Assisted High-Harmonic Generation in Graphene. *Nat. Commun.* **2017**, *8*, 14380.
(57) Malard, L. M.; Alencar, T. V.; Barboza, A. P. M.; Mak, K. F.; de Paula, A. M. Observation of Intense Second Harmonic Generation from MoS_2 Atomic Crystals. *Phys. Rev. B: Condens. Matter Mater. Phys.* **2013**, *87*, 201401.
(58) Kumar, N.; Najmaei, S.; Cui, Q.; Ceballos, F.; Ajayan, P. M.; Lou, J.; Zhao, H. Second Harmonic Microscopy of Monolayer MoS_2. *Phys. Rev. B: Condens. Matter Mater. Phys.* **2013**, *87*, 161403.

https://doi.org/10.1021/acsnano.1c03775
ACS Nano 2021, 15, 13415−13426

(59) Chen, H.; Corboliou, V.; Solntsev, A. S.; Choi, D.-Y.; Vincenti, M. A.; de Ceglia, D.; de Angelis, C.; Lu, Y.; Neshev, D. N. Enhanced Second-Harmonic Generation from Two-Dimensional $MoSe_2$ on a Silicon Waveguide. *Light: Sci. Appl.* **2017**, *6*, No. e17060.
(60) Janisch, C.; Wang, Y.; Ma, D.; Mehta, N.; Elías, A. L.; Perea-López, N.; Terrones, M.; Crespi, V.; Liu, Z. Extraordinary Second Harmonic Generation in Tungsten Disulfide Monolayers. *Sci. Rep.* **2015**, *4*, 5530.
(61) Wang, G.; Marie, X.; Gerber, I.; Amand, T.; Lagarde, D.; Bouet, L.; Vidal, M.; Balocchi, A.; Urbaszek, B. Giant Enhancement of the Optical Second-Harmonic Emission of WSe_2 Monolayers by Laser Excitation at Exciton Resonances. *Phys. Rev. Lett.* **2015**, *114*, 097403.
(62) Säynätjoki, A.; Karvonen, L.; Rostami, H.; Autere, A.; Mehravar, S.; Lombardo, A.; Norwood, R. A.; Hasan, T.; Peyghambarian, N.; Lipsanen, H.; Kieu, K.; Ferrari, A. C.; Polini, M.; Sun, Z. Ultra-Strong Nonlinear Optical Processes and Trigonal Warping in MoS_2 Layers. *Nat. Commun.* **2017**, *8*, 893.
(63) Woodward, R. I.; Murray, R. T.; Phelan, C. F.; de Oliveira, R. E. P.; Runcorn, T. H.; Kelleher, E. J. R.; Li, S.; de Oliveira, E. C.; Fechine, G. J. M.; Eda, G.; de Matos, C. J. S. Characterization of the Second-and Third-Order Nonlinear Optical Susceptibilities of Monolayer MoS_2 Using Multiphoton Microscopy. *2D Mater.* **2017**, *4*, 011006.
(64) Fan, X.; Jiang, Y.; Zhuang, X.; Liu, H.; Xu, T.; Zheng, W.; Fan, P.; Li, H.; Wu, X.; Zhu, X.; Zhang, Q.; Zhou, H.; Hu, W.; Wang, X.; Sun, L.; Duan, X.; Pan, A. Broken Symmetry Induced Strong Nonlinear Optical Effects in Spiral WS_2 Nanosheets. *ACS Nano* **2017**, *11*, 4892−4898.
(65) Dekorsy, T.; Yakovlev, V. A.; Seidel, W.; Helm, M.; Keilmann, F. Infrared-Phonon−Polariton Resonance of the Nonlinear Susceptibility in GaAs. *Phys. Rev. Lett.* **2003**, *90*, 055508.
(66) Paarmann, A.; Razdolski, I.; Gewinner, S.; Schöllkopf, W.; Wolf, M. Effects of Crystal Anisotropy on Optical Phonon Resonances in Midinfrared Second Harmonic Response of SiC. *Phys. Rev. B: Condens. Matter Mater. Phys.* **2016**, *94*, 134312.
(67) Nicoletti, D.; Cavalleri, A. Nonlinear Light−Matter Interaction at Terahertz Frequencies. *Adv. Opt. Photonics* **2016**, *8*, 401−464.
(68) Winta, C. J.; Gewinner, S.; Schöllkopf, W.; Wolf, M.; Paarmann, A. Second-Harmonic Phonon Spectroscopy of α-Quartz. *Phys. Rev. B: Condens. Matter Mater. Phys.* **2018**, *97*, 094108.
(69) Cartella, A.; Nova, T. F.; Fechner, M.; Merlin, R.; Cavalleri, A. Parametric Amplification of Optical Phonons. *Proc. Natl. Acad. Sci. U. S. A.* **2018**, *115*, 12148−12151.
(70) Li, P.; Dolado, I.; Alfaro-Mozaz, F. J.; Casanova, F.; Hueso, L. E.; Liu, S.; Edgar, J. H.; Nikitin, A. Y.; Vélez, S.; Hillenbrand, R. Infrared Hyperbolic Metasurface Based on Nanostructured van der Waals Materials. *Science* **2018**, *359*, 892−896.
(71) Li, P.; Hu, G.; Dolado, I.; Tymchenko, M.; Qiu, C.-W.; Alfaro-Mozaz, J. F.; Casanova, F.; Hueso, L. E.; Liu, S.; Edgar, J. H.; Vélez, S.; Alu, A.; Hillenbrand, R. Collective Near-Field Coupling and Nonlocal Phenomena in Infrared-Phononic Metasurfaces for Nano-Light Canalization. *Nat. Commun.* **2020**, *11*, 1−8.
(72) Yuan, Z.; Chen, R.; Li, P.; Nikitin, A. Y.; Hillenbrand, R.; Zhang, X. Extremely Confined Acoustic Phonon Polaritons in Monolayer-hBN/Metal Heterostructures for Strong Light-Matter Interactions. *ACS Photonics* **2020**, *7*, 2610−2617.
(73) Li, N.; Guo, X.; Yang, X.; Qi, R.; Qiao, T.; Li, Y.; Shi, R.; Li, Y.; Liu, K.; Xu, Z.; Liu, L.; García de Abajo, F. J.; Dai, Q.; Wang, E.-G.; Gao, P. Direct Observation of Highly Confined Phonon Polaritons in Suspended Monolayer Hexagonal Boron Nitride. *Nat. Mater.* **2021**, *20*, 43−48.
(74) Giles, A. J.; Dai, S.; Vurgaftman, I.; Hoffman, T.; Liu, S.; Lindsay, L.; Ellis, C. T.; Assefa, N.; Chatzakis, I.; Reinecke, T. L.; Tischler, J. G.; Fogler, M. M.; Edgar, J. H.; Basov, D. N.; Caldwell, J. D. Ultralow-Loss Polaritons in Isotopically Pure Boron Nitride. *Nat. Mater.* **2018**, *17*, 134−139.
(75) Sohier, T.; Gibertini, M.; Calandra, M.; Mauri, F.; Marzari, N. Breakdown of Optical Phonons' Splitting in Two-Dimensional Materials. *Nano Lett.* **2017**, *17*, 3758−3763.
(76) Rokuta, E.; Hasegawa, Y.; Suzuki, K.; Gamou, Y.; Oshima, C. Phonon Dispersion of an Epitaxial Monolayer Film of Hexagonal Boron Nitride on Ni(111). *Phys. Rev. Lett.* **1997**, *79*, 4609−4612.
(77) Cai, Q.; Scullion, D.; Falin, A.; Watanabe, K.; Taniguchi, T.; Chen, Y.; Santos, E. J. G.; Li, L. H. Raman Signature and Phonon Dispersion of Atomically Thin Boron Nitride. *Nanoscale* **2017**, *9*, 3059−3067.
(78) Tajaddodianfar, F.; Yazdi, M. R. H.; Pishkenari, H. N. Nonlinear Dynamics of MEMS/NEMS Resonators: Analytical Solution by the Homotopy Analysis Method. *Microsyst. Technol.* **2017**, *23*, 1913−1926.
(79) Birnbaum, K. M.; Boca, A.; Miller, R.; Boozer, A. D.; Northup, T. E.; Kimble, H. J. Photon Blockade in an Optical Cavity with One Trapped Atom. *Nature* **2005**, *436*, 87−90.
(80) Manjavacas, A.; Nordlander, P.; García de Abajo, F. J. Plasmon Blockade in Nanostructured Graphene. *ACS Nano* **2012**, *6*, 1724−1731.
(81) Koppens, F. H. L.; Chang, D. E.; García de Abajo, F. J. Graphene Plasmonics: A Platform for Strong Light-Matter Interactions. *Nano Lett.* **2011**, *11*, 3370−3377.
(82) Stehle, Y.; Meyer, H. M., III; Unocic, R. R.; Kidder, M.; Polizos, G.; Datskos, P. G.; Jackson, R.; Smirnov, S. N.; Vlassiouk, I. V. Synthesis of Hexagonal Boron Nitride Monolayer: Control of Nucleation and Crystal Morphology. *Chem. Mater.* **2015**, *27*, 8041−8047.
(83) Maruyama, M.; Okada, S. Energetics and Electronic Structure of Triangular Hexagonal Boron Nitride Nanoflakes. *Sci. Rep.* **2018**, *8*, 16657.
(84) Valerius, P.; Herbig, C.; Will, M.; Arman, M. A.; Knudsen, J.; Caciuc, V.; Atodiresei, N.; Michely, T. Annealing of Ion-Irradiated Hexagonal Boron Nitride on Ir(111). *Phys. Rev. B: Condens. Matter Mater. Phys.* **2017**, *96*, 235410.
(85) Hattori, Y.; Taniguchi, T.; Watanabe, K.; Nagashio, K. Anisotropic Dielectric Breakdown Strength of Single Crystal Hexagonal Boron Nitride. *ACS Appl. Mater. Interfaces* **2016**, *8*, 27877−27884.
(86) Kim, S.; Fröch, J. E.; Gardner, A.; Li, C.; Aharonovich, I.; Solntsev, A. S. Second-Harmonic Generation in Multilayer Hexagonal Boron Nitride Flakes. *Opt. Lett.* **2019**, *44*, 5792−5795.
(87) Shan, Y.; Li, Y.; Huang, D.; Tong, Q.; Yao, W.; Liu, W.-T.; Wu, S. Stacking Symmetry Governed Second Harmonic Generation in Graphene Trilayers. *Sci. Adv.* **2018**, *4*, No. eaat0074.
(88) Autere, A.; Jussila, H.; Marini, A.; Saavedra, J. R. M.; Dai, Y.; Säynätjoki, A.; Karvonen, L.; Yang, H.; Amirsolaimani, B.; Norwood, R. A.; Peyghambarian, N.; Lipsanen, H.; Kieu, K.; García de Abajo, F. J.; Sun, Z. Optical Harmonic Generation in Monolayer Group-VI Transition Metal Dichalcogenides. *Phys. Rev. B: Condens. Matter Mater. Phys.* **2018**, *98*, 115426.
(89) Hao, Q.; Yi, H.; Su, H.; Wei, B.; Wang, Z.; Lao, Z.; Chai, Y.; Wang, Z.; Jin, C.; Dai, J.; Zhang, W. Phase Identification and Strong Second Harmonic Generation in Pure ϵ-Inse and Its Alloys. *Nano Lett.* **2019**, *19*, 2634−2640.
(90) Nikogosyan, D. N. *Nonlinear Optical Crystals: A Complete Survey*; Springer-Verlag: New York, 2005.
(91) Harasaki, A.; Kato, K. New Data on the Nonlinear Optical Constant, Phase-Matching, and Optical Damage of $AgGaS_2$. *Jpn. J. Appl. Phys.* **1997**, *36*, 700.
(92) Shoji, I.; Kondo, T.; Kitamoto, A.; Shirane, M.; Ito, R. Absolute Scale of Second-Order Nonlinear-Optical Coefficients. *J. Opt. Soc. Am. B* **1997**, *14*, 2268−2294.
(93) Popkova, A. A.; Antropov, I. M.; Fröch, J. E.; Kim, S.; Aharonovich, I.; Bessonov, V. O.; Solntsev, A. S.; Fedyanin, A. A. Optical Third-Harmonic Generation in Hexagonal Boron Nitride Thin Films. *ACS Photonics* **2021**, *8*, 824−831.
(94) Jiang, T.; Huang, D.; Cheng, J.; Fan, X.; Zhang, Z.; Shan, Y.; Yi, Y.; Dai, Y.; Shi, L.; Liu, K.; Zeng, C.; Zi, J.; Sipe, J. E.; Shen, Y.-R.; Liu, W.-T.; Wu, S. Gate-Tunable Third-Order Nonlinear Optical Response of Massless Dirac Fermions in Graphene. *Nat. Photonics* **2018**, *12*, 430.

https://doi.org/10.1021/acsnano.1c03775
ACS Nano 2021, 15, 13415−13426

(95) Cui, Q.; Muniz, R. A.; Sipe, J.; Zhao, H. Strong and Anisotropic Third-Harmonic Generation in Monolayer and Multilayer ReS_2. *Phys. Rev. B: Condens. Matter Mater. Phys.* **2017**, *95*, 165406.
(96) Bloembergen, N.; Burns, W. K.; Matsuoka, M. Reflected Third Harmonic Generated by Picosecond Laser Pulses. *Opt. Commun.* **1969**, *1*, 195−198.
(97) Burns, W. K.; Bloembergen, N. Third-Harmonic Generation in Absorbing Media of Cubic or Isotropic Symmetry. *Phys. Rev. B* **1971**, *4*, 3437.
(98) Watkins, D.; Phipps, C.; Thomas, S. Determination of the Third-Order Nonlinear Optical Coefficients of Germanium through Ellipse Rotation. *Opt. Lett.* **1980**, *5*, 248−249.
(99) Demetriou, G.; Bookey, H. T.; Biancalana, F.; Abraham, E.; Wang, Y.; Ji, W.; Kar, A. K. Nonlinear Optical Properties of Multilayer Graphene in the Infrared. *Opt. Express* **2016**, *24*, 13033−13043.
(100) Liu, L.; Xu, K.; Wan, X.; Xu, J.; Wong, C. Y.; Tsang, H. K. Enhanced Optical Kerr Nonlinearity of MoS_2 on Silicon Waveguides. *Photonics Res.* **2015**, *3*, 206−209.
(101) Wang, K.; Feng, Y.; Chang, C.; Zhan, J.; Wang, C.; Zhao, Q.; Coleman, J. N.; Zhang, L.; Blau, W. J.; Wang, J. Broadband Ultrafast Non-Linear Absorption and Non-Linear Refraction of Layered Molybdenum Dichalcogenide Semiconductors. *Nanoscale* **2014**, *6*, 10530−10535.
(102) Dong, N.; Li, Y.; Zhang, S.; McEvoy, N.; Zhang, X.; Cui, Y.; Zhang, L.; Duesberg, G. S.; Wang, J. Dispersion of Nonlinear Refractive Index in Layered WS_2 and WSe_2 Semiconductor Films Induced by Two-Photon Absorption. *Opt. Lett.* **2016**, *41*, 3936−3939.
(103) Yang, T.; Abdelwahab, I.; Lin, H.; Bao, Y.; Rong Tan, S. J.; Fraser, S.; Loh, K. P.; Jia, B. Anisotropic Third-Order Nonlinearity in Pristine and Lithium Hydride Intercalated Black Phosphorus. *ACS Photonics* **2018**, *5*, 4969−4977.
(104) Jia, L.; Wu, J.; Yang, T.; Jia, B.; Moss, D. J. Large Third-Order Optical Kerr Nonlinearity in Nanometer-Thick $PdSe_2$ 2D Dichalcogenide Films: Implications for Nonlinear Photonic Devices. *ACS Appl. Nano Mater.* **2020**, *3*, 6876−6883.
(105) Cox, J. D.; Yu, R.; García de Abajo, F. J. Analytical Description of the Nonlinear Plasmonic Response in Nanographene. *Phys. Rev. B: Condens. Matter Mater. Phys.* **2017**, *96*, 045442.
(106) Hage, F. S.; Radtke, G.; Kepaptsoglou, D. M.; Lazzeri, M.; Ramasse, Q. M. Single-Atom Vibrational Spectroscopy in the Scanning Transmission Electron Microscope. *Science* **2020**, *367*, 1124−1127.
(107) Kresse, G.; Furthmüller, J. Efficient Iterative Schemes for *ab Initio* Total-Energy Calculations Using a Plane-Wave Basis Set. *Phys. Rev. B: Condens. Matter Mater. Phys.* **1996**, *54*, 11169−11186.
(108) Kresse, G.; Hafner, J. *Ab Initio* Molecular Dynamics for Liquid Metals. *Phys. Rev. B: Condens. Matter Mater. Phys.* **1993**, *47*, 558−561R.
(109) Kresse, G.; Furthmüller, J. Efficiency of *ab Initio* Total Energy Calculations for Metals and Semiconductors Using a Plane-Wave Basis Set. *Comput. Mater. Sci.* **1996**, *6*, 15−50.
(110) Blöchl, P. E. Projector Augmented-Wave Method. *Phys. Rev. B: Condens. Matter Mater. Phys.* **1994**, *50*, 17953.
(111) Perdew, J. P.; Burke, K.; Ernzerhof, M. Generalized Gradient Approximation Made Simple. *Phys. Rev. Lett.* **1996**, *77*, 3865−3868.

https://doi.org/10.1021/acsnano.1c03775
ACS Nano 2021, 15, 13415−13426